ACS NANO
Cite This: ACS Nano 2018, 12, 5030–5041
www.acsnano.org

ARTICLE

High-Performance Ultrathin Active Chiral Metamaterials

Zilong Wu,[†] Xiaodong Chen,[‡] Mingsong Wang,[†] Jianwen Dong,[‡] and Yuebing Zheng*,[†]

[†]Department of Mechanical Engineering, Materials Science and Engineering Program, and Texas Materials Institute, The University of Texas at Austin, Austin, Texas 78712, United States

[‡]School of Physics and State Key Laboratory of Optoelectronic Materials and Technologies, Sun Yat-sen University, Guangzhou 510275, China

Supporting Information

ABSTRACT: Ultrathin active chiral metamaterials with dynamically tunable and responsive optical chirality enable new optical sensors, modulators, and switches. Herein, we develop ultrathin active chiral metamaterials of highly tunable chiroptical responses by inducing tunable near-field coupling in the metamaterials and exploit the metamaterials as ultrasensitive sensors to detect trace amounts of solvent impurities. To demonstrate the active chiral metamaterials mediated by tunable near-field coupling, we design moiré chiral metamaterials (MCMs) as model metamaterials, which consist of two layers of identical Au nanohole arrays stacked upon one another in moiré patterns with a dielectric spacer layer between the Au layers. Our simulations, analytical fittings, and experiments reveal that spacer-dependent near-field coupling exists in the MCMs, which significantly enhances the spectral shift and line shape change of the circular dichroism (CD) spectra of the MCMs. Furthermore, we use a silk fibroin thin film as the spacer layer in the MCM. With the solvent-controllable swelling of the silk fibroin thin films, we demonstrate actively tunable near-field coupling and chiroptical responses of the silk-MCMs. Impressively, we have achieved the spectral shift over a wavelength range that is more than one full width at half-maximum and the sign inversion of the CD spectra in a single ultrathin (1/5 of wavelength in thickness) MCM. Finally, we apply the silk-MCMs as ultrasensitive sensors to detect trace amounts of solvent impurities down to 200 ppm, corresponding to an ultrahigh sensitivity of >10^5 nm/refractive index unit (RIU) and a figure of merit of 10^5/RIU.

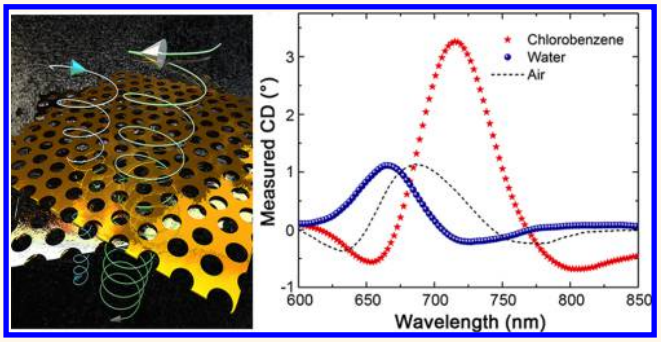

KEYWORDS: *active chiral metamaterials, moiré patterns, Fano resonance, electromagnetically induced transparency, silk fibroin*

Chiral molecules such as amino acids and proteins are the building blocks of life. Optical activities such as circular dichroism (CD) and optical rotation dispersion (ORD) arise from the disparity in interactions of the chiral molecules with left-handed circularly polarized (LCP) light and right-handed circularly polarized (RCP) light. The understanding of the optical chirality in natural molecules has led to chiral metamaterials with exceptionally strong optical activities.[1−8] In particular, the sophisticated engineering of the interactions between photonic nanostructures has led to chiral metamaterials with near-unity CD and extraordinary rotation of linearly polarized lights, paving the way toward a wide range of ultracompact chiroptical devices such as broadband circular polarizers, chiral sensors, metamirrors, and circularly polarized radiation sources.[9−17]

Ultrathin active chiral metamaterials with their dynamically tunable and responsive optical chirality enable new devices and applications.[18−20] For example, active modulation of optical handedness, that is, CD sign inversion, underpins applications such as polarization engineering and information storage.[21,22] Modulation of resonant wavelengths in CD spectra, typically by at least one full width at half-maximum (fwhm),[23,24] can enhance the applications in optical sensors and spectroscopy.[25] So far, the CD spectral shift has been regulated by the refractive index of the surroundings of the metamaterials[25] and by the optical handedness by the structural handedness.[26,27] However, these approaches have encountered challenges in inverting the optical chirality of simple planarized metamaterials for compact chiroptical devices. It is even more challenging to achieve both active modulation of spectral shift and the reversible inversion of chiroptical responses in single metamaterials, which are qualities desired for chiroptical devices such as metamirrors and stereo displays. In addition, to generate strong CD often

Received: April 6, 2018
Accepted: April 30, 2018
Published: April 30, 2018

DOI: 10.1021/acsnano.8b02566
ACS Nano 2018, 12, 5030–5041

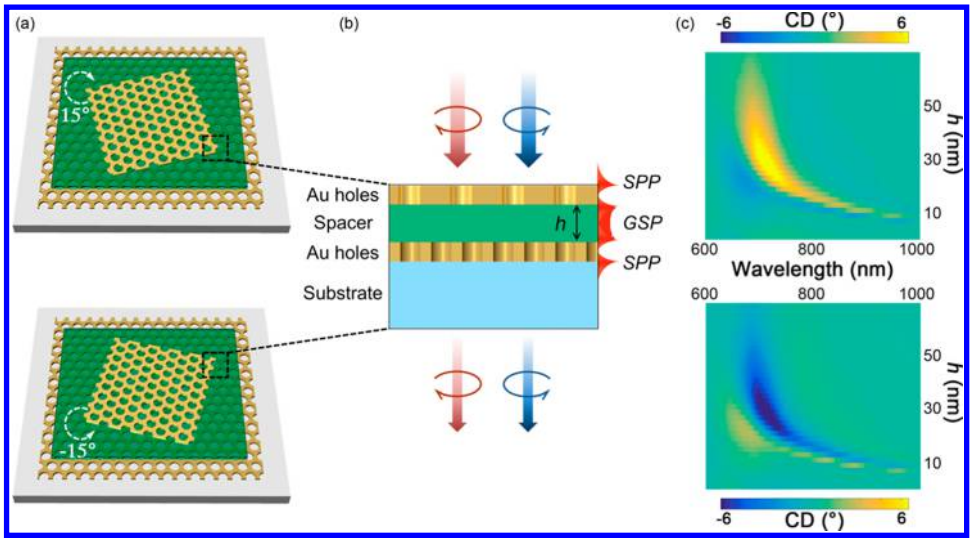

Figure 1. Design of chiral metamaterials that support tunable near-field coupling. (a) Perspective views of right-handed (RH) (top panel) and left-handed (LH) (bottom panel) MCMs with the relative in-plane rotation angles of 15° and −15°, respectively. (b) Cross-sectional view of the MCMs where surface plasmons are excited by circularly polarized light. Red: Left-handed circularly polarized (LCP) light. Blue: Right-handed circularly polarized (RCP) light. (c) Simulated CD spectra of RH (top panel) and LH (bottom panel) MCMs as a function of spacer thickness (h). The MCMs are embedded in a homogeneous environment where the refractive indices of the dielectric spacer layer (n_{spacer}), the substrate ($n_{substrate}$), and the superstrate ($n_{superstrate}$) are equal to 1.46. The CD values are described in ellipticity (θ), that is, θ (degree) = 32.98 × ($T_{LCP} - T_{RCP}$).[29,30]

requires multiple layers of unit cells, making the metamaterials too bulky to be applied in ultracompact devices.

To overcome these challenges, we explore an alternative mechanism—tunable near-field coupling—to realize ultrathin active chiral metamaterials for high performance applications. Specifically, the active chiral metamaterials exhibit the active control of the optical handedness and the precisely controlled CD spectral shift over a wavelength range that is more than one fwhm. To demonstrate the conception and application of the active chiral metamaterials, we have organized the Results and Discussion of this paper into four subsections. In the first subsection, we design chiral metamaterials that not only support near-field coupling that can be highly tuned in a convenient manner but also can be fabricated at large scale and high efficiency. Our design leads to moiré chiral metamaterials (MCMs) which consist of two layers of identical Au nanohole arrays stacked into moiré patterns with a dielectric spacer layer in between. As discussed in the second subsection, our numerical, analytical, and experimental studies reveal that the MCMs support near-field coupling between different plasmonic modes, which can be described by Fano resonance and a coupled oscillator model. Controlling the spacer thickness of the MCMs tunes the near-field coupling which in turn enhances the optical chirality of the MCMs.

In the third subsection, we introduce a silk fibroin thin film into the MCM as the spacer layer to demonstrate the active chiral metamaterials. Silk fibroin is a natural protein from the *Bombyx mori* cocoon that exhibits precisely controllable swelling caused by solvent up-take. With the solvent-controllable swelling of the silk fibroin thin films as the spacer layers, we demonstrate actively tunable near-field coupling and chiroptical responses of the silk-MCMs using different solvents and their mixtures. We have achieved a spectral shift over a wavelength range that is more than one fwhm. In the same device, we have also demonstrated the active control of the optical chirality, including the ON/OFF switching of CD values and the inversion of CD sign at the peak or dip wavelengths of the silk-MCMs. In the last subsection, we apply the silk-MCMs as ultrasensitive sensors to detect trace amounts of solvent impurities. We have shown that our silk-MCMs can detect trace amounts of water (0.1% v/v) in isopropyl alcohol (IPA) and methanol (200 ppm) in hexane, corresponding to an ultrahigh sensitivity of >10^5 nm/RIU and a figure of merit of 10^5/RIU.

RESULTS AND DISCUSSION

Design of Chiral Metamaterials That Support Tunable Near-Field Coupling. When designing model systems, we keep in mind chiral metamaterials that not only support near-field coupling that are highly tunable in a convenient and precise manner but also can be experimentally fabricated at large scale and high efficiency for their practical applications. Based on these criteria, we choose the MCMs where the structural chirality is transferred to chiroptical responses when two layers of achiral plasmonic nanohole arrays are stacked together with a relative in-plane rotation to form moiré patterns.[28] Plasmonic nanohole arrays exhibit extraordinary optical properties such as strong localization of electromagnetic waves and enhanced optical transmission. Herein, we insert a thin dielectric spacer between the two rotated plasmonic Au nanohole arrays (Figure 1) to induce near-field coupling in the chiral metamaterials. As detailed in the next subsection, the near-field coupling arises from the interaction between surface plasmon modes at the outer surfaces of the Au nanohole arrays and the inner Au-dielectric interfaces.

As shown in Figure 1a, each of the MCMs consists of two layers of identical Au nanohole arrays with triangular lattices separated by a dielectric spacer. We defined the MCMs as right-handed (RH) (top panel in Figure 1a) when the top layer of Au nanohole array has a 15° in-plane rotation relative to the bottom layer and *vice versa* (bottom panel in Figure 1a). As illustrated in Figure 1b, surface plasmon polaritons (SPPs) can be generated at the Au-dielectric interfaces by incident light.[31] The incorporation of a dielectric spacer layer between the two Au nanohole arrays enables the generation of gap surface

DOI: 10.1021/acsnano.8b02566
ACS Nano 2018, 12, 5030−5041

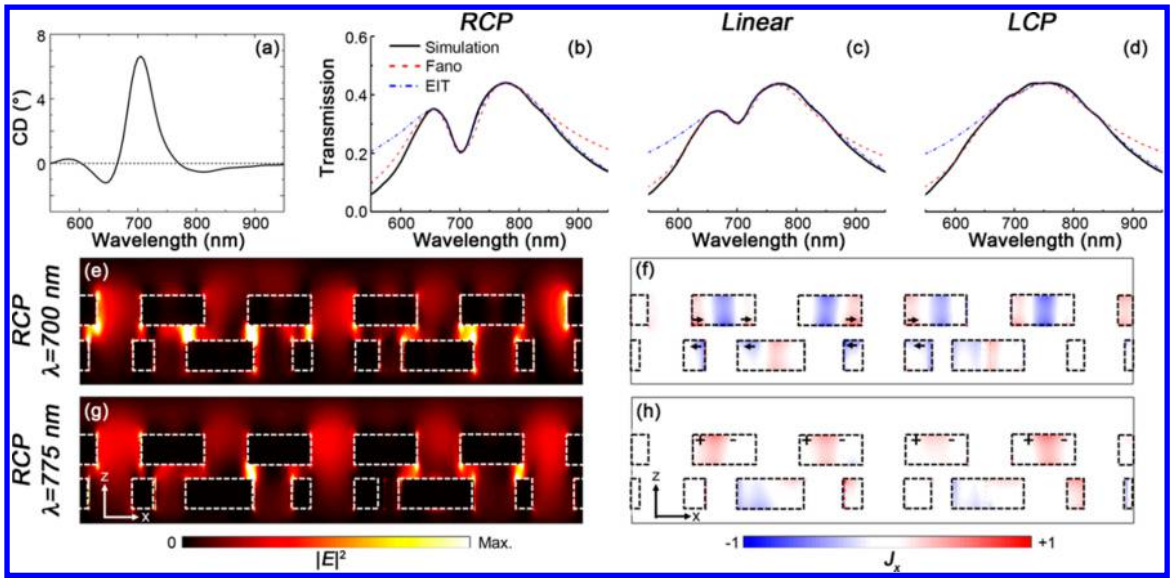

Figure 2. Optical simulations and analytical fitting reveal the critical role of near-field coupling in the enhanced chiroptical responses of the MCMs. (a) CD spectrum of the RH MCM with a spacer thickness of 30 nm. (b–d) Optical transmission spectra of the RH MCM under (b) RCP, (c) linearly polarized, and (d) LCP incident light obtained from FDTD simulations (black solid curves), Fano fitting (red dashed curves), and EIT model fitting (blue dash-dot curves). (e–h) Cross-sectional view of simulated mapping of (e, g) normalized electric intensity $|E|^2$ and (f, h) normalized current density (J_x) in the RH MCM under RCP light at the wavelength of (e, f) 700 nm and (g, h) 775 nm. The dashed lines mark the cross sections of the Au nanohole arrays. The arrows in (f) show four pairs of antiparallel surface currents, indicating the antibonding (dark) mode under RCP light at the wavelength of 700 nm. No obvious antiparallel surface currents are observed in (h), indicating diminished dark modes at the wavelength of 775 nm. The (+) and (−) signs in (h) illustrate the dipolar charge distributions in the top layer of Au nanohole arrays, indicating the bonding (bright) mode at the wavelength of 775 nm. The in-plane rotation angle between top and bottom Au nanohole arrays was 15°.

plasmons (GSPs) or internal SPPs.[32] The resonant wavelength of the GSPs can be described as[32]

$$\lambda_{GSP} = \frac{2\pi}{|\vec{G}|}\sqrt{\varepsilon_s}\left[\frac{h}{h + \lambda_p \coth(k_p d)/\pi}\right]^{-1/2} \quad (1)$$

where the $|\vec{G}|$ is the reciprocal lattice vector of the nanohole array, ε_s and h are the dielectric function and the thickness of the dielectric spacer layer, d is the thickness of the metal layers, and $k_p = 2\pi/\lambda_p = \omega_p/c$, where ω_p and c are the plasma frequency of the metal and the vacuum light speed. As can be obtained from eq 1, the resonant wavelength of the GSPs can be effectively modulated by spacer thickness h. In contrast, the resonant wavelength of the SPPs can be described as[32,33]

$$\lambda_{SPP} = \frac{D}{(n_x^2 + n_y^2)^{1/2}}\left(\frac{\varepsilon_i \varepsilon_m}{\varepsilon_i + \varepsilon_m}\right)^{1/2} \quad (2)$$

where the ε_i and ε_m are dielectric functions of the environment and the metal. From eq 2, the resonant wavelength of SPPs does not vary with spacer thickness h. Therefore, we can efficiently tune the spectral overlap and thus the coupling efficiency between the SPPs and GSP in the MCM by controlling the spacer thickness h. Benefiting from the nanoholes and the ultrathin thickness (<1/10 of resonant wavelength) of the Au thin films, hybridization can occur between the fields generated by SPPs and GSPs, as detailed in next subsection. Guided by eqs 1 and 2, we designed the structures of MCMs to introduce near-field coupling, which enhances the transfer of the structural chirality to the optical chirality in the MCMs. We have modulated the near-field coupling and thus the chiroptical responses of the MCMs by tuning the thickness (h) of the dielectric spacer layer.

To reveal the effects of the dielectric spacer layer on the optical chirality of the MCMs, we have simulated the CD spectra using a finite-difference time-domain (FDTD) method. Figure 1c shows the simulated CD spectra of the RH (top panel) and LH (bottom panel) MCMs when the spacer thickness varies from 0 to 70 nm. The in-plane rotation angles (−15° and 15°) were optimized to achieve the strongest optical chirality (Figure S1). The RH and LH MCMs show identical spectral line shapes with opposite CD values at all spacer thicknesses. The optical chirality of the MCMs is significantly enhanced by the existence of the dielectric spacer, as shown in Figure S2, where the CD spectra of RH MCMs without spacer and with a 30 nm dielectric spacer are compared. A further study of the CD spectra reveals that both amplitude and peak (or dip) wavelength are effectively modulated by the spacer thickness. Specifically, an increased spacer thickness makes a blue shift in the CD peak (or dip) wavelength. A large shift of 160 nm occurs when the spacer thickness changes from 10 to 70 nm. A large CD value occurs at a spacer thickness of ~25 nm, where the optical chirality of 42°/μm is among the largest values that have been reported so far.[34]

Mechanistic Studies on Chiroptical Responses Mediated by Near-Field Coupling. We have applied optical simulations and analytical fitting to reveal the physical mechanisms behind the tunable and enhanced chiroptical responses of the MCMs. We start with the RH MCM with a spacer thickness of 30 nm, where the strongest chiroptical responses appear, as shown in Figure 1c. Figure 2a–d shows the CD spectrum of the RH MCM as well as the transmission spectra under RCP, linearly polarized, and LCP light. A large asymmetric transmission dip appears near λ = 700 nm on the simulated RCP transmission spectrum (black solid curve) in Figure 2b, indicating the strong near-field coupling between

DOI: 10.1021/acsnano.8b02566
ACS Nano 2018, 12, 5030–5041

plasmonic modes in the RH MCM under RCP incident light. In contrast, both the asymmetry and the amplitude of the transmission dip are largely reduced for linear polarization and nearly eliminated for LCP light, as shown in Figure 2c,d. We believe that the polarization-dependent near-field coupling in the MCM causes the large difference between the LCP and RCP transmission, leading to the strong optical chirality near the coupling wavelength, as shown in Figure 2a.

We have further revealed the near-field origins of the coupling shown in Figure 2b. Figure 2e shows the cross-sectional view of simulated mapping of normalized electric field intensity $|E|^2$ in the RH MCM at a wavelength of 700 nm under RCP incident light. The large number of strong hot spots in the spacer layer indicates that strong GSPs are excited at this wavelength, which correspond to the transmission dip in Figure 2b. In contrast, the hot spots are largely diminished in the spacer layer at a wavelength of 775 nm under RCP incident light, while the propagating SPPs at the holes of the top Au layer become more obvious, as shown in Figure 2g. Figure 2f shows the cross-sectional view of the simulated mapping of normalized current density (J_x) in the RH MCM at a wavelength of 700 nm under RCP incident light. Four pairs of antiparallel surface currents (as marked by arrows) are observed, indicating the mirrored charge distribution between the two Au-spacer interfaces. The mirrored charge distribution has led to the antibonding (dark) mode supported by the GSPs. Similar antibonding modes have also been observed in the dielectric spacers between two layers of plasmonic structures in metal-insulator-metal metamaterials.[35,36] In contrast, no obvious antiparallel currents are observed in the normalized current density distribution at a wavelength of 775 nm, as shown in Figure 2h. The (+) and (−) signs in Figure 2h show the dipolar charge distributions in the top layer of Au nanohole arrays, indicating the bonding (bright) mode supported by the SPPs. The SPP-related bright mode has been studied for extraordinary optical transmission through metal nanohole arrays.[37,38]

Furthermore, we have investigated analytically the plasmonic coupling in the MCMs. In plasmonic systems, the coupling between the bright and the dark modes leads to a Fano resonance, featuring the asymmetric transmission dip in Figure 2b.[39−41] The Fano resonances are well-studied as the consequence of spectral and spatial overlap between a superradiant (bright) mode and a subradiant (dark) mode.[39−41] The spectra of Fano resonances in plasmonic systems can be mathematically fitted by the product of a symmetric resonance (σ_s) and an asymmetric resonance (σ_a):[36]

$$\sigma_t(\omega) = \sigma_s(\omega)\sigma_a(\omega) \tag{3}$$

The symmetric resonance (σ_s) and the asymmetric resonance (σ_a) can be obtained by[36]

$$\sigma_s(\omega) = \frac{a^2}{\left(\frac{\omega^2 - \omega_s^2}{2W_s\omega_s}\right)^2 + 1} \tag{4}$$

$$\sigma_a(\omega) = \frac{\left(\frac{\omega^2 - \omega_a^2}{2W_a\omega_a} + q\right)^2 + b}{\left(\frac{\omega^2 - \omega_a^2}{2W_a\omega_a}\right)^2 + 1} \tag{5}$$

where a, ω_s, and W_s are the maximum resonance amplitude, the central spectral position, and spectral width of the symmetric resonance, respectively, ω_a and W_a are the central spectral position and spectral width of the asymmetric resonance, respectively, and q and b are the asymmetric parameter and the modulation damping parameter in Fano resonances, respectively. Using eqs 3−5, we can fit the transmission spectra to retrieve the coupling parameters that lead to the asymmetric line shape. The fitted spectrum of transmission of the RH MCM under RCP light using the Fano model is shown as the red dashed curve in Figure 2b. The good match between the Fano fitting and the simulation confirms the Fano resonance due to the plasmonic bright and dark modes in the MCMs. The details and parameters of the Fano fitting are described in section 3 of the Supporting Information.

We have further demonstrated the polarization dependence of the Fano resonance. The red dashed curves in Figure 2c,d show the Fano fitting for the transmission of the RH MCM under linearly polarized and LCP incident light. Table 1 shows

Table 1. Fitting Parameters for Curves in Figure 2 Based on the Fano Resonance and EIT Model

coupling parameters		RCP	linear	LCP
Fano model	q	0.095	0.07	0.02
EIT model	κ ($\times 10^{-2}$)	10.0	6.5	1.9

the values of the Fano parameter q retrieved from the fitting. The Fano parameter q for the RCP incident light is approximately 5 times that for the LCP incident light, indicating the larger asymmetry in transmission spectrum under RCP incident light. As expected, the q value for linearly polarized incident light is between the RCP and LCP ones since the linearly polarized light is regarded as the combination of RCP and LCP light. The complete parameters of the Fano fitting are described in section 3 of Supporting Information. From our analytical fitting, we conclude that the Fano resonances in MCMs highly depend on the chirality of incident light, leading to the large chiroptical responses of the MCMs.

It is worthy of noticing that the transmission spectrum in Figure 2b shows the feature of an optical coupling phenomenon known as electromagnetically induced absorption (EIA), which is an analogue of electromagnetically induced transmission (EIT).[42−44] We refer to such phenomenon as EIT in this article for consistency. It has been reported that under special conditions, the Fano resonance can be viewed as EIT.[45,46] In such cases, both Fano and EIT can explain the plasmonic coupling in a same structure.[43,44,47] The coupling between bright and dark modes in EIT can be understood by a coupled oscillator model, which was applied to study the optical chirality in plasmonic systems.[42,48] In contrast to the Fano resonance, which focuses on the spectral asymmetry, the coupled oscillator model directly provides the coupling strength between the plasmonic modes. Therefore, to estimate the coupling strength between the bright and dark modes in MCMs and its influence on the optical chirality, we have fitted the transmission spectra in Figure 2b−d using the coupled oscillator model.[42,43] The bright and dark modes in this model are described by[42,43]

$$\omega_b^{-2}\ddot{p}(t) + \gamma_b\omega_b^{-1}\dot{p}(t) + p(t) = f(t) - \tilde{\kappa}q(t) \tag{6}$$

$$\omega_d^{-2}\ddot{q}(t) + \gamma_d\omega_d^{-1}\dot{q}(t) + q(t) = -\tilde{\kappa}p(t) \tag{7}$$

where $p(t)$, ω_b, and γ_b are the excitation, resonance frequency, and damping factor of the bright mode, respectively, $q(t)$, ω_d,

DOI: 10.1021/acsnano.8b02566
ACS Nano 2018, 12, 5030−5041

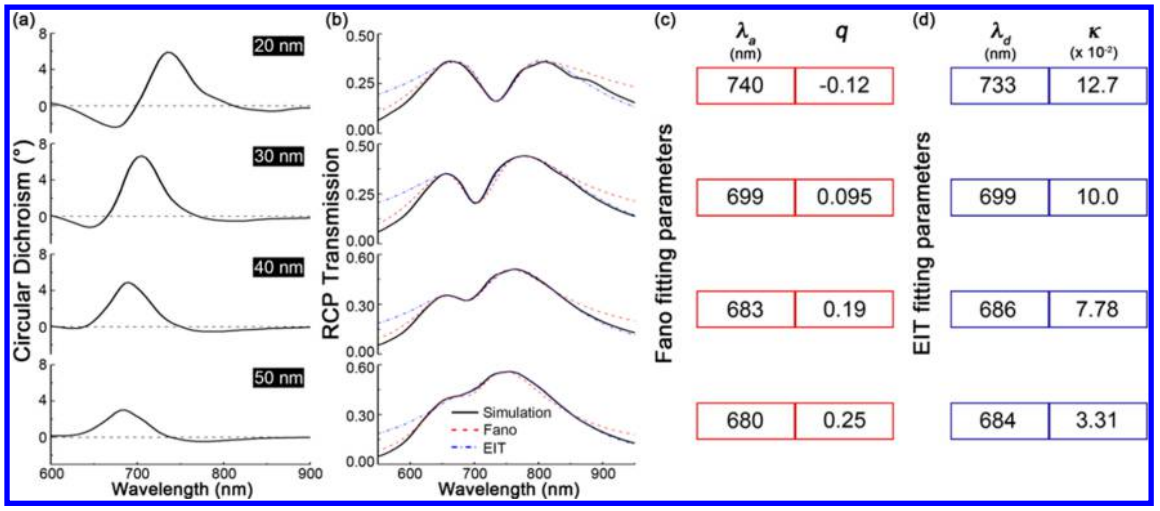

Figure 3. Optical simulations and analytical fittings reveal the critical role of near-field coupling in the tunable chiroptical responses of the MCMs. (a) CD spectra of the RH MCMs of the variable spacer thicknesses, that is, 20, 30, 40, and 50 nm. (b) Three types of optical transmission spectra of the RH MCMs of the variable spacer thicknesses corresponding to (a), which are obtained from simulation (black solid curves), Fano fitting (red dashed curves), and EIT fitting (blue dash-dot curves). (c, d) Fitting parameters from (c) Fano and (d) EIT models for the RH MCMs of the variable spacer thicknesses corresponding to (a). The in-plane rotation angle between top and bottom Au nanohole arrays was 15°.

and γ_d are the excitation, resonance frequency, and damping factor of the dark mode, respectively, and $f(t)$ is the external force that excites the bright mode. The coupling strength between the bright and the dark modes is described as a constant $\tilde{\kappa}$. A phase shift between the bright and dark mode is considered in the complex coupling constant $\tilde{\kappa} = \kappa e^{-i(\theta-\phi)}$. Considering that the optical transmission of plasmonic nanohole arrays arises from the scattered light by the nanholes,[49,50] we derive an expression of the transmission by solving the eqs 6 and 7, as detailed in section 4 of Supporting Information. The expression is applied to fit the simulated spectra, as shown in Figure 2b–d. Table 1 summarizes the coupling constant κ derived from the coupled oscillator model. The coupling constant for the RCP light is approximately 5 times that of the LCP light with the constant for the linear polarization light between them. The fitting from the coupled oscillator model indicates that the strong optical chirality in MCMs can be attributed to the polarization-dependent coupling strength between the bright and the dark modes. The complete fitting parameters using the coupled oscillator model are described in section 4 of Supporting Information.

We attribute the tunable chiroptical responses to the spacer-dependent near-field coupling in the MCMs. As shown in Figure 3a,b, both the CD spectra and the near-field coupling (*i.e.*, the transmission dips in the spectra of Figure 3b) highly depend on the spacer thickness of the MCMs. Figure 3b shows that the increased spacer thickness leads to a blue shift in the transmission dip of the RH MCMs under RCP incident light. The spacer-dependent near-field coupling arises from the dependence of the GSPs on the spacer thickness, as predicted by eq 1, which is an analogy of a LC circuit model.[51,52] In contrast, the SPPs at the outer surfaces of the Au nanohole arrays do not depend on the spacer thickness, as predicted by eq 2. Therefore, the spectral overlap between the dark modes and the bright modes varies when the spacer layer thickness is changed, leading to the tunable chiroptical responses. The variations of the dark mode and the near-field coupling at the different spacer thickness are verified by the space-dependent fitting parameters from both Fano and EIT models (Figure 3c,d), which are retrieved from the fitting in Figure 3b. The fitting parameters in the coupled oscillator model clearly demonstrate the variation in coupling strength between the bright and the dark modes in the MCMs. At the spacer thickness of 20 and 30 nm, strong EIT phenomena occur due to the large coupling strength in the MCMs, as indicated by the large κ values in Figure 3d. The small Fano parameter q (*i.e.*, close to 0) in the RH MCM with the spacer thickness of 20 and 30 nm confirms the existence of EIT phenomena.[45,46] The small difference between the asymmetric resonance wavelength λ_a in the Fano model and the dark mode wavelength λ_d in the EIT model is attributed to the collective excitation of the bright and dark modes that leads to the asymmetric resonance.[36] The complete fitting parameters are described in sections 3 and 4 of Supporting Information.

The spacer-dependent coupling and the resulting chiroptical responses are also observed in the simulated scattering and absorption spectra, as shown in Figure S3. Both scattering and absorption spectra show a large discrepancy between LCP and RCP incident light near the coupling wavelength. It is worthy of noticing that the scattering spectra in Figure S3 have similar features to the transmission spectra in Figures 2 and 3, confirming that the transmission of the plasmonic nanohole arrays arises from the scattered light by the nanoholes.[49,50]

Another important factor in the spacer-dependent near-field coupling is the dephasing time (T) of the Fano resonance, which impacts applications in energy conversion, optical switches, and sensors.[53−55] From the Fano fitting in Figure 3b, we have obtained the dephasing time of the induced Fano dip by $T = 2\hbar/\Gamma$, where the Γ is the line width of the asymmetric resonance in Fano fitting.[55] Table S2 shows the dephasing time T of the asymmetric resonances at variable spacer thickness. The increase of the spacer thickness from 20 to 40 nm leads to a decrease of the dephasing time T from 11 to 8.3 fs, indicating the increase of radiative damping in the MCMs.[55] As a result, the Fano dip is broadened with the increase of the spacer thickness. The larger dephasing time for the MCM with a spacer thickness of 20 nm also indicates the stronger electromagnetic field confinement in the MCM,

DOI: 10.1021/acsnano.8b02566
ACS Nano 2018, 12, 5030−5041

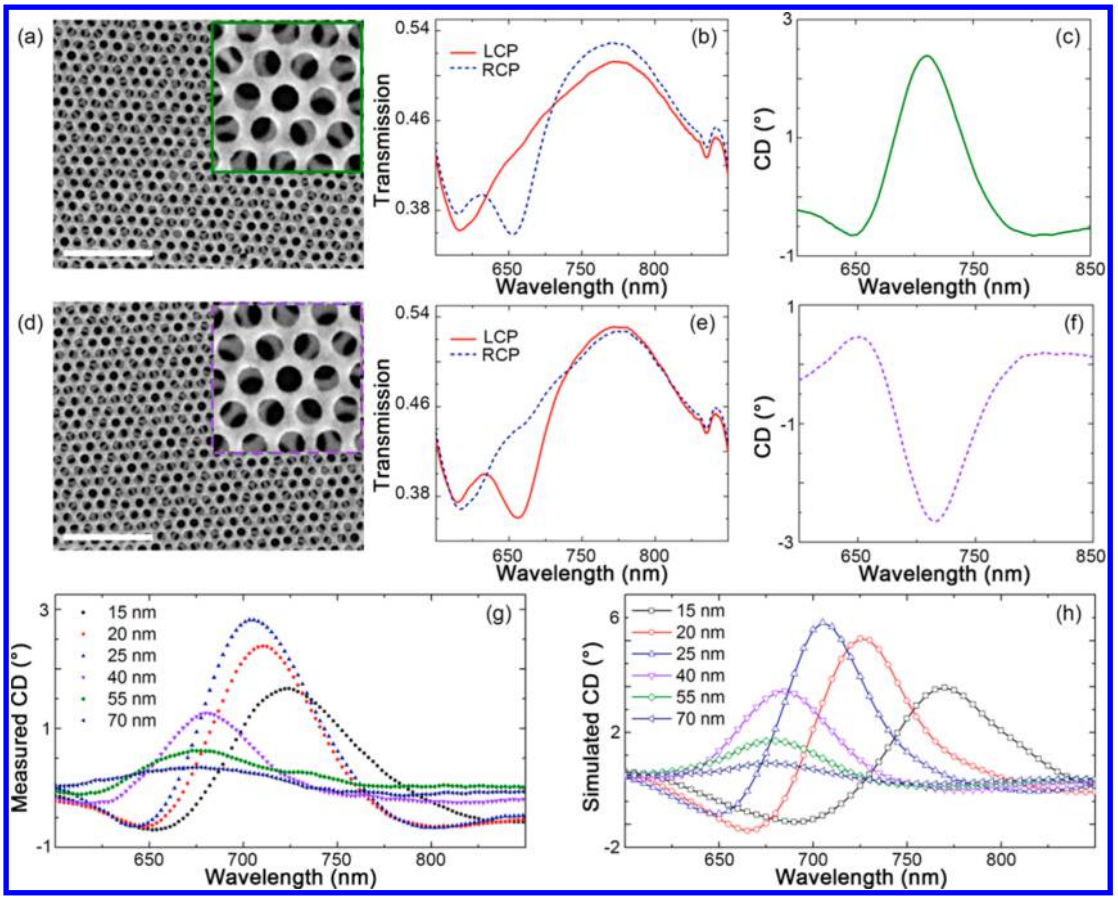

Figure 4. Experimental demonstrations of the near-field coupling and the optical chirality of the MCMs. (a, d) SEM images of the RH and LH MCMs. The scale bars are 2 μm. (b, e) Measured optical transmission spectra of the RH and LH MCMs under the LCP and RCP light irradiation. The spacer thickness is 20 nm. (c, f) Measured CD spectra of the RH and LH MCMs. The spacer thickness is 20 nm. (g, h) Measured and simulated CD spectra of the RH MCMs of various spacer thicknesses.

leading to the better sensing applications.[56] It is worthy of noticing that, when the spacer thickness is above 40 nm, the increase of dephasing time does not lead to the more prominent Fano dip, as shown in Table S2 and Figure 3b. This effect is attributed to the significantly enhanced energy loss to metallic structures, which is parametrized by the increased value of b parameter in the Fano resonance,[36] as shown in Table S2.

We have further elucidated how the near-field coupling affects the CD line shapes of the MCMs. As shown in Figure 3a, the line shapes for the MCMs with the spacer thicknesses below 30 nm exhibit the bipolar characteristics of static coupling, which is related to the helical oscillator model.[28,48] Specifically, when the thickness of the spacer layer in MCMs is small, the interlayer near-field coupling is strong, as indicated by the analytical fitting in Figure 3. Therefore, the perturbations from the electrostatic fields exerted by the other Au layer are strong, as described in the static coupling mechanism. The line shapes for the MCMs with the thicker spacer layers (≥40 nm) exhibit dynamic coupling, which is related to Born−Kuhn model.[48] Specifically, in dynamic coupling, the perturbations are attributed to electrodynamic radiation from the other Au layers in the chiral environment under the influences of incident light. In the case of MCMs, the near-field coupling is weakened when the thickness of the spacer layer is above 40 nm, as indicated by the analytical fitting in Figure 3. Therefore, the electrodynamic radiation from the top layer becomes dominant.

We have experimentally verified the simulations on the tunable optical chirality of the MCMs. For this purpose, we fabricated MCMs of precisely controllable spacer thickness (see Supporting Information section 5 and Methods). As examples, Figure 4a,d shows the scanning electron microscopy (SEM) images of the RH and LH MCMs with the relative in-plane rotation angles of 15° and −15°, respectively. The Au nanohole arrays have lattice constants and thicknesses of 300 and 60 nm, respectively. The thickness of the dielectric spacer, which is a thin layer of spin-on glass (IC1-200, Futurrex Inc.), is ∼20 nm. Figure 4b,e shows the optical transmission spectra of the RH and LH MCMs under RCP and LCP light irradiation. The corresponding CD spectra are shown in Figure 3c,f. We clearly observe the near-field coupling ("RCP" curve in Figure 4b and "LCP" curve in Figure 4e) and the strong optical chirality, as predicted by our simulations in Figure 2.

We have further verified the dependence of the optical chirality on the spacer thickness. Figure 4g,h shows the measured and simulated CD spectra of the RH MCMs with the variable spacer thicknesses from 15 to 70 nm. The good match between the measured and simulated spectra confirms the large tunability of the optical chirality by the thickness of the dielectric spacer. The measured CD spectra make blue shifts to the simulated spectra when the spacer thickness is smaller than 20 nm. Such discrepancies between the measured and

DOI: 10.1021/acsnano.8b02566
ACS Nano 2018, 12, 5030−5041

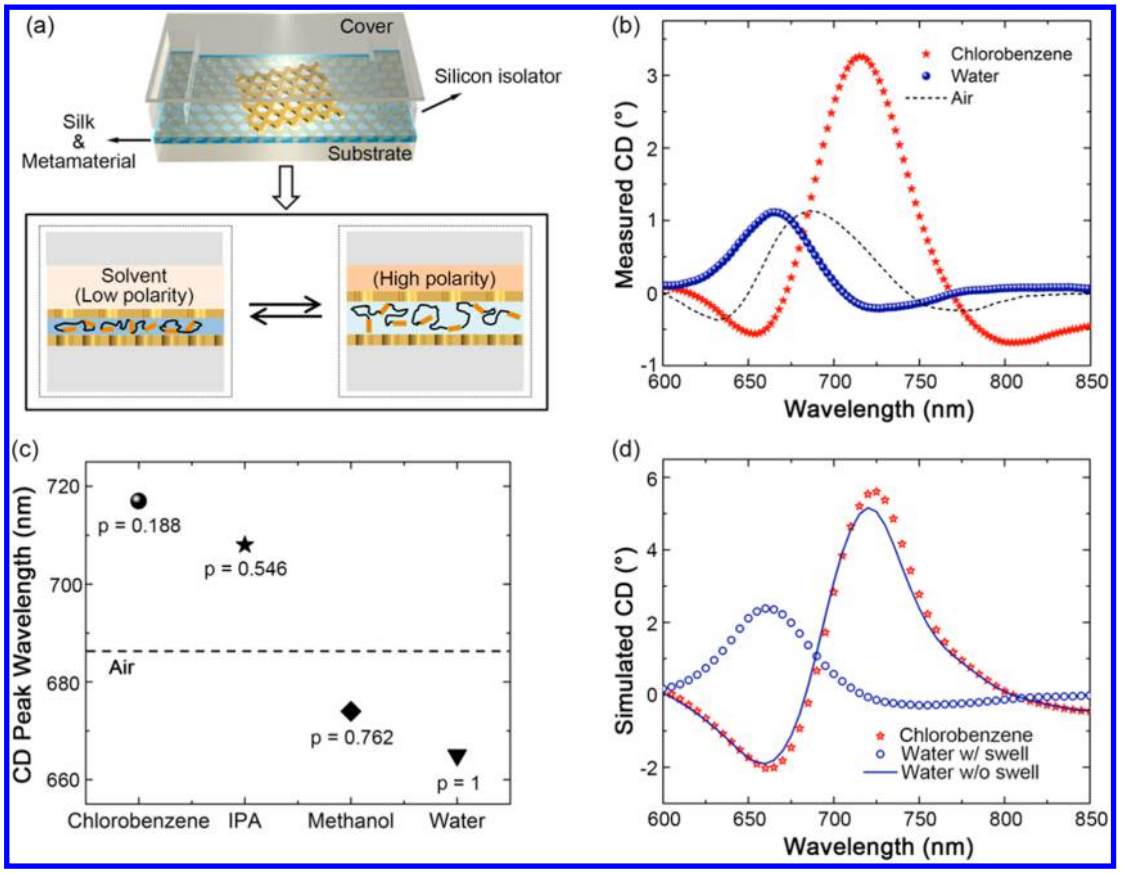

Figure 5. Active chiral metamaterials where silk thin films serve as the spacer layers in the MCMs. (a) Top panel: A perspective view of a silk-MCM integrated into a microfluidic cell. Bottom panel: A cross-sectional illustration of the reversible tuning of the silk thickness by solvent polarity. (b) Measured CD spectra of a RH silk-MCM exposed to air (black dashes), chlorobenzene (red stars), and water (blue circles). (c) Measured CD peak wavelengths of the RH silk-MCM exposed to chlorobenzene, IPA, methanol, and water. The solvent polarity values (p) are given below the symbols. The CD peak wavelength of the silk-MCM in air is marked by the dashed line as a reference. (d) Simulated CD spectra of the RH silk-MCM exposed to chlorobenzene (red stars) and water (blue circles). 30% thickness expansion of the silk spacer was considered when chlorobenzene was changed to water. The CD spectrum of the silk-MCM exposed to water, but without the swelling of the silk spacer, was also simulated as a reference (blue solid curve).

simulated spectra are attributed to the increased surface roughness of the dielectric spacer with the reduced thickness. We can precisely tune the spacer thickness and thus the chiroptical responses of the MCMs by RIE time, as shown in Figure S5.

Demonstration of Active Chiral Metamaterials. With the knowledge of the spacer-dependent optical chirality of the MCMs, we further demonstrate dynamically tunable MCMs by using thin films of silk fibroin protein as spacers. The silk fibroin extracted from the *Bombyx mori* cocoon exhibits excellent bonding with Au surfaces[57] to form a uniform thin film between the Au nanohole arrays. It also undergoes highly controllable swelling behavior in response to the polarity of surrounding solvents. Details on the fabrication of the silk-MCMs are available in Supporting Information section 6.1 and Figure S6. We built a microfluidic cell to deliver various solvents onto the top of the silk-MCMs (*i.e.*, superstrate), as shown in the top panel of Figure 5a. The as-prepared silk spacer had a thickness of ~25 nm, which is determined by atomic force microscopy. As shown in the bottom panel of Figure 5a, the hydrogel-like silk fibroin can swell up to 60% in volume when exposed to solvents of high polarity.[57,58] The swelling is highly reversible upon a change in the solvent polarity.

We measured the chiroptical responses of the silk-MCMs exposed to solvents of different polarities. Figure 5b shows the measured CD spectra of the RH silk-MCM exposed to chlorobenzene and deionized water. The CD spectrum of the RH silk-MCM exposed to air was also measured and shown as a reference. If only considering the effects of refractive index (without the spacer expansion) on the CD spectra, one would expect a continuous red shift in the CD peak wavelength when the sample was subsequently exposed to air, water, and chlorobenzene due to their increased refractive indices, that is, air (n = 1), water (n = 1.333), and chlorobenzene (n = 1.53). Surprisingly, a blue shift in the CD peak wavelength was observed when we changed air to water. We hypothesize that a substantial change in the thickness of the silk spacer layer would play a critical role in the CD behavior of the MCMs exposed to the different solvents.

We furthered our experiments and simulations to test our hypothesis and to understand the physics behind the observed effects of the different solvents on the CD spectra of the silk-MCMs. We measured the CD spectra of the silk-MCMs exposed to more types of solvents with the different polarities, including chlorobenzene, IPA, methanol, and water (Figure S7). Figure 5c compares the measured CD peak wavelengths of a single silk-MCM subsequently exposed to the various solvents. The values of solvent polarity (p) are also given in

DOI: 10.1021/acsnano.8b02566
ACS Nano 2018, 12, 5030−5041

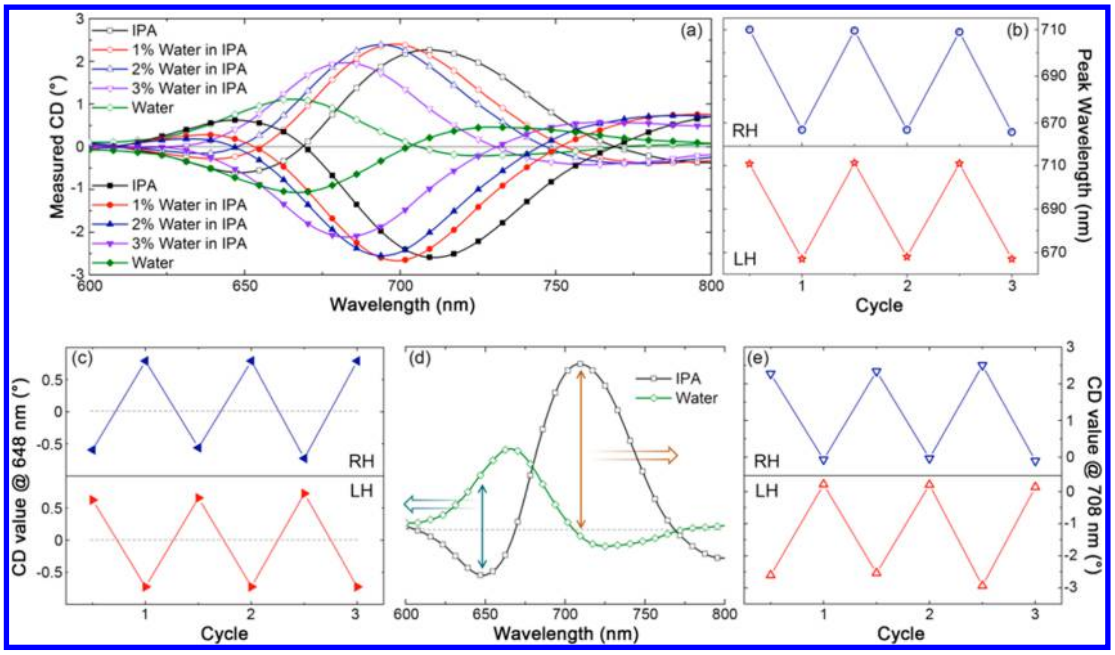

Figure 6. A precise and reversible modulation of the optical chirality of the silk-MCMs by the water-IPA mixtures. (a) A precise tuning of the CD spectra of the RH (top panel) and LH (bottom panel) silk-MCMs by controlling the water-IPA ratio. (b) Reversible shifts of the CD peak (top panel) and dip (bottom panel) wavelengths of the RH (top panel) and LH (bottom panel) silk-MCMs being alternatively exposed to IPA and water for three cycles. (c) Reversible inversion of chiroptical responses at a wavelength of 648 nm when the silk-MCMs were alternatively exposed to IPA and water for three cycles. The horizontal dashed lines indicate a CD value of 0. (d) CD spectra of the RH silk-MCM exposed to IPA and water, respectively. The arrows indicate where the data in (c) and (e) were collected. The horizontal dashed line indicates a CD value of 0. (e) Reversible ON/OFF switching of the CD values at a wavelength of 708 nm when the silk-MCMs were alternatively exposed to IPA and water for three cycles. The top and bottom panels in (c) and (e) are for the RH and LH silk-MCMs, respectively.

Figure 5c. A dashed line marks the measured CD peak wavelength when the silk-MCM was exposed to air. Chlorobenzene (p = 0.188) and IPA (p = 0.546) solvents with relatively low polarity caused little change in the silk spacer layer. Thus, the effects of the refractive index dominated the CD spectral changes. Accordingly, the higher refractive indices of chlorobenzene (n = 1.53) and IPA (n = 1.378) led to a continuous red shift in the CD peak wavelength when the exposed environment of the silk-MCM was changed from air to IPA to chlorobenzene. In contrast, the polarities of methanol (p = 0.762) and water (p = 1) were large enough to cause significant swelling of the spacer layer due to the up-take of the solvent molecules by the silk matrix. The expanded silk spacer (compared with the silk spacer exposed to air) led to a blue shift in the CD peak wavelength, which dominated over the effects of the refractive index on the CD spectra.

We have further confirmed the critical role of spacer expansion in the tuning of the chiroptical responses of the silk-MCMs based on the simulations of the CD spectra. According to our experimental measurements in Figure 5b, we assumed that there was no change in silk spacer layer when the silk-MCM was exposed to chlorobenzene. We set the initial thickness and refractive index of the silk spacer layer as 25 nm (determined by atomic force microscopy) and 1.5. When the silk-MCM was exposed to water, the silk spacer layer expanded by 30% in thickness, leading to a final spacer thickness of 50 nm with a refractive index of 1.4.[58] As shown in Figure 5d, the CD spectrum underwent a large blue shift in the peak wavelength with a decreased CD value when the exposure environment of the silk-MCM was changed from chlorobenzene to water, matching well with the measured CD spectra in Figure 5b. We also simulated the CD spectra of the silk-MCM on the condition that there was no spacer expansion when the exposure environment of the silk-MCM was changed from chlorobenzene to water. As shown in Figure 5d, little change would occur to the CD spectrum if there was no spacer expansion upon the exposure of the silk-MCM to water. Thus, our simulations support our hypothesis that the large tunability of the chiroptical responses of the silk-MCMs is enabled by the controllable silk spacer thickness in response to the solvents, which modulates the near-field coupling.

By taking advantage of the high sensitivities of the silk spacer thickness to the solvent polarity and of the optical chirality to the spacer thickness, we have further demonstrated a fine control of the CD spectra of silk-MCMs that were exposed to various water-IPA mixtures. The ratio of water and IPA in the mixture precisely controls the polarity and thus the swelling of the silk spacer layer. Figure 6a shows the measured CD spectra of the RH (top panel) and LH (bottom panel) silk-MCMs exposed to pure IPA, 1% water in IPA, 2% water in IPA, 3% water in IPA, and pure water, respectively. The increased ratio of water in IPA expanded the silk spacer thickness from 25 to 50 nm, leading to a continuous blue shift of the CD peak (or dip) wavelength from ~710 nm to ~665 nm. The CD peak shift was reversible as a function of the water-IPA ratio. Figure 6b shows the three-cycle reversible peak shifts of the RH (top panel) and LH (bottom panel) silk-MCMs being alternatively exposed to IPA and water.

We have further analyzed the reversible modulation of CD values and the inversion of chiroptical responses at the specific wavelengths, as shown in Figure 6c–e. Figure 6d shows the measured CD spectra of the RH silk-MCM exposed to IPA and water, respectively. As indicated by the brown double arrow, the CD value at a wavelength of 708 nm changed from the

DOI: 10.1021/acsnano.8b02566
ACS Nano 2018, 12, 5030–5041

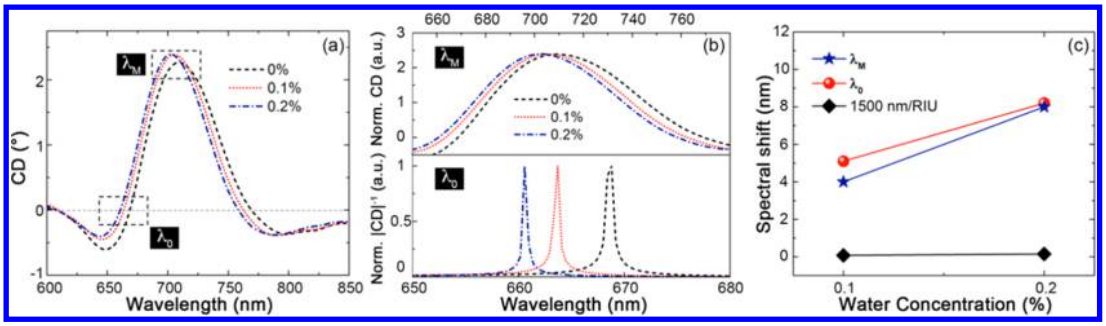

Figure 7. Ultrasensitive detection of water impurity in IPA based on the optical chirality of the silk-MCMs. (a) A series of CD spectra of the RH silk-MCM subsequently exposed to water-IPA mixtures with the ultralow water concentrations of 0%, 0.1%, and 0.2%, respectively. (b) Top panel: Normalized zoom-in CD spectra around the wavelength of λ_M as indicated by a dashed square in Figure 6a. Bottom panel: Normalized zoom-in $|CD|^{-1}$ spectra around the wavelength of λ_0, including the zero-crossing points, as indicated by a dashed square in (a). (c) Shifts of λ_M and λ_0 as a function of water concentration in the water-IPA mixtures. For a comparison, the spectral shift as a function of water concentration for a conceptual refractive-index sensor with the state-of-the-art sensitivity of 1500 nm/RIU is also shown.

maximum value (~2.6°) for IPA to ~0° for water. Thus, we could reversibly switch ON and OFF the optical chirality at the wavelength of 708 nm by an alternative exposure of the silk-MCMs to IPA and water, as shown in Figure 6e. Since the silk-MCMs have an ultrathin thickness of 150 nm, we obtain a large modulation depth of ~17.3°/μm. The alternative exposure to chlorobenzene and water further increases the modulation depth up to ~25°/μm, which is among the largest modulation depths reported for active chiral materials.[18,25,59]

To further our excitement, we can even achieve an inversion of CD sign at a wavelength of 648 nm when the exposure environment was changed from IPA to water, as indicated by the cyan double arrow in Figure 6d. Figure 6c shows the reversible inversion of the CD values between ~ −0.6° and ~0.7° at the wavelength of 648 nm when the silk-MCMs were alternatively exposed to IPA and water for three cycles. For the planar metamaterials, previous demonstrations of the inversion of chiroptical responses have been limited to those with complex structures and large thickness. With an ultrathin thickness of ~150 nm and the well-defined moiré structure, our silk-MCMs will open up new opportunities for ultracompact devices.

As an initial effort, we show how the reversible large-depth modulation of the CD values of the silk-MCMs can benefit applications that exploit circularly polarized imaging. Using a digital camera combined with a 650 nm long pass filter, we have demonstrated the reversible ON/OFF switching of color contrast between the LH and RH enantiomers in the silk-MCMs that were under LCP (or RCP) light illumination and alternatively exposed to IPA and water. Please refer to Supporting Information section 7 and Figure S8 for the more details. When a 650 nm short pass filter was applied, we were able to visualize the flip of the color contrast between the LH and RH silk-MCMs that were under LCP (or RCP) light illumination and alternatively exposed to IPA and water, as shown in Supporting Information section 8 and Figure S9. Such a versatile and vivid control of color contrast under the circularly polarized light illumination is highly relevant to applications such as stereo displays.

Ultrasensitive Detection of Solvent Contamination. The high sensitivity of the optical chirality of the MCMs to the spacer thickness underpins the development of a variety of sensors. For any targeted analytes, one would select spacer materials that can change their thickness in response to the desired analytes. For the silk-MCMs, we take advantage of the high sensitivity of the silk thickness to solvent polarity and demonstrate the ultrasensitive detection of trace amount of solvent impurities, including water impurity in IPA and methanol impurity in hexane.

Water molecules are often regarded as impurity in many high-grade liquids such as purified organic chemicals, oil, and lubricants. A trace amount of water impurity (<1%) in the lubricants or chemicals can lead to degradation of precise instruments and mechanical devices or cause problems in chemical synthesis. Therefore, it is highly desired to develop the ultrasensitive detection of water contamination in the high-grade nonpolar liquids during their storage, transportation, and usage. Optical sensors have advantages over chemical counterparts in remote and high-sensitivity detection methods. However, a trace amount of solvent impurities usually causes little change in refractive index of the solvents, which makes many powerful refractive-index-based optical sensors such as plasmonic sensors and photonic crystal sensors ineffective in the impurity detection. Our optical sensors that exploit the optical chirality of the MCMs enhanced by the near-field coupling can overcome this limitation.

As an initial demonstration, we have shown that the silk-MCMs enable the ultrasensitive detection of water impurity in IPA. Figure 7a shows a series of CD spectra of the RH silk-MCM when subsequently exposed to various water-IPA mixtures with the water concentrations of 0%, 0.1%, and 0.2% in volume. We apply two algorithms to interrogate the CD spectra for the quantitative analyses of the water impurity. One is shown in the top panel of Figure 7b, which exhibits the normalized zoom-in CD spectra around the wavelength of λ_M as indicated by a dashed square in Figure 7a. λ_M is located between 680 and 720 nm. The other is shown in the bottom panel of Figure 7b, which exhibits the normalized zoom-in $|CD|^{-1}$ spectra[60] around the wavelength of λ_0, as indicated by a dashed square in Figure 7a. λ_0 is located between 660 and 680 nm, which covers the zero-crossing points.

Both panels in Figure 7b reveal that λ_0 and λ_M make continuous blue shifts when the water concentration is increased gradually. As shown in Figure 7c, tracking λ_0 and λ_M shifts from the CD spectra of our silk-PCMM offers a superior sensitivity when compared to a conventional refractive-index sensor with the state-of-the-art performance. At an impurity level of 0.1% water, our sensitivities based on λ_0 and λ_M are 1×10^5 nm/RIU and 8×10^4 nm/RIU, respectively. In contrast, the conventional refractive-index sensor experi-

DOI: 10.1021/acsnano.8b02566
ACS Nano 2018, 12, 5030−5041

ences little spectral shift due to the extremely small refractive-index change ($\Delta n \sim 5 \times 10^{-5}$) caused by the low-concentrated water impurity in IPA. In addition, as shown in Figure 7b, tracking λ_0 provides a figure-of-merit (FOM) of $\sim 1 \times 10^5$ /RIU, which is ~70 times higher than the FOM (~1455/RIU) from tracking λ_M. The higher FOM arises from an extremely narrow fwhm of ~0.8 nm (bottom panel of Figure 7b) in comparison to a fwhm of ~55 nm (top panel of Figure 7b).

In a similar way, we have demonstrated the ultrasensitive detection of methanol in hexane. As shown in Figure S10, we can easily detect methanol with a volume percentage of 0.02% (*i.e.*, 200 ppm) and even below. This demonstration indicates the capability of the silk-MCMs in detecting a trace amount of alcohol impurity in a high-purity lubricant or oil, which is crucial to many industrial applications.

We have further analyzed the theoretical sensitivity limit of the sensor based on the silk-MCMs. In the silk-MCMs, the spectral shifts for high-performance sensing are due to the large blue shifts of the GSPs caused by the polarity-dependent swelling of the silk spacer. When applying the spectral shifts of propagating surface plasmons for sensing, the sensitivity limit can be obtained by analyzing the minimum detectable change in the resonance wave vector dk_r:[61]

$$\lim(dk_r) = \frac{1.3Nn_0^3k_0\varepsilon_i}{\varepsilon_r^2} \tag{8}$$

where n_0 and k_0 are the refractive index of the dielectric environment and the wave vector of incident light, ε_i and ε_r are the imaginary and real part of the permittivity of the plasmonic material, and N is a dimensionless quantity describing the noise of the experiments, which is defined as

$$N = \frac{\text{noise equivalent (optical) power at receiver}}{\text{optical power of incident probe beam}} \tag{9}$$

In the silk-MCM, which is a double-layer plasmonic nanohole array with a silk dielectric spacer, the propagation of GSPs, which are known as internal SPPs, is described as[32]

$$k_{GSP} = k_0 n_s \left[\frac{h + \lambda_p \coth(k_p d)/\pi}{h}\right]^{1/2} \tag{10}$$

where n_s and h are the refractive index and the thickness of the dielectric spacer layer, d is the thickness of the metal layers, and $k_p = 2\pi/\lambda_p = \omega_p/c$, where ω_p and c are the plasma frequency of the metal and the vacuum light speed. Combining eqs 8 and 10, we obtain the following relation:

$$\lim\left[dh \times \frac{\left(-\frac{1}{2}k_0 n_s \lambda_p \coth(k_p d)/\pi\right)}{h^2\sqrt{1 + \frac{\lambda_p \coth(k_p d)/\pi}{h}}}\right] = \frac{1.3Nn_s^3k_0\varepsilon_i}{\varepsilon_r^2} \tag{11}$$

Therefore, the sensing limit of our silk-MCMs can be described in terms of the minimum detectable changes in spacer layer thickness:

$$\lim(dh) = \frac{-2.6Nn_s^2\varepsilon_i}{\varepsilon_r^2}\sqrt{\frac{h^3(h + X)}{X^2}} \tag{12}$$

where $X = \lambda_p \coth(k_p d)/\pi$. For the solvent sensing with our silk-MCM, $n_s = 1.4$, $h = 25$ nm, $d = 60$ nm, and $\omega_p = 2.1 \times 10^{15}$ Hz. At an initial wavelength (~700 nm) of the GSP, we consider the ε_i and ε_r of Au as 1.1 and −16.5, respectively. Using $N \approx 10^{-3}$ for typical experiments,[61] we obtain a sensitivity limit in the minimum detectable change of spacer thickness $\lim(dh) \approx 9 \times 10^{-14}$ m. Such a small value indicates the ultrahigh sensitivity of our sensors based on silk-MCMs. A tiny change in the thickness of the silk spacer layer caused by the uptake of solvent impurities can lead to a substantial spectral shift in the optical spectra. The sensitivity limit in terms of contaminant percentage depends on the specific type of solvent impurities and the difference in polarity values between the solvents and impurities. Eq 12 can guide us on the further developments of ultrasensitive sensors based on the variation of spacer thickness in MCMs. For example, decreasing the initial spacer thickness or choosing active materials with the smaller refractive index as the spacer can further increase the sensitivity.

CONCLUSIONS

In summary, near-field coupling is effective in enhancing and tuning the optical chirality of chiral metamaterials. This innovation pioneers a new category of active chiral metamaterials that exhibit a large modulation depth. With their spacer-sensitive near-field coupling, ultrathin thickness and compatibility with large-scale high-throughput fabrication, our model systems, that is, MCMs with dielectric spacer layers, feature tremendous advantages for various device applications such as active metamirrors, tunable optical polarizers, and sensors. Specifically, we have shown that the high sensitivity of near-field coupling to the spacer thickness in the MCMs enables the strong modulation of the chiroptical responses. The physical mechanisms behind the spacer-dependent near-field coupling have also been revealed through analytical fitting. The active MCMs that include functional silk fibroin thin films as spacer layers are well suited for high performance uses including the ON/OFF switching of CD values and the handedness inversion of the optical chirality in response to the solvent polarity. Such silk-MCMs have been applied as sensors to detect solvent impurities with an ultrahigh sensitivity (down to 200 ppm) and an extremely large FOM ($\sim 1 \times 10^5$/RIU). We could apply the MCM sensors to various types of analytes by incorporating the functional spacer layers that change their volumes in response to the targeted analytes. The near-field coupling concept is general and can be extended to other types of chiral metamaterials for both chiral enhancements and active functionalities.

METHODS

Materials and Sample Preparation. We fabricated various chiral metamaterials by combining nanosphere lithography and wet-transfer processing (see details in Supporting Information and Figure S4). Polystyrene (PS) spheres with a diameter of 300 nm were purchased from Thermo Scientific Inc. (5030A). Thermal evaporation was applied to deposit Au to form nanohole arrays. Electron beam evaporation was applied to deposit Cu sacrifice layer. The O_2 plasma etching of the PS spheres was performed on a reactive ion etcher (March Plasma CS170IF) using a flow rate of 20 sccm and a power of 60 W. The SF_6 plasma etching of the spin-on glass (IC1-200, Futurrex Inc.) was conducted at a flow rate of 20 sccm and a power of 60 W. All other chemicals were purchased from Fisher Scientific Inc. unless otherwise specified. The microfluidic cell of 9 mm in diameter and 0.5 mm in depth was made of a Press-to-Seal silicone isolator (Invitrogen, Inc.) and covered by a glass slide.

Optical Characterizations. The optical transmission spectra were measured by optical microspectroscopy that integrates a spectrometer (Andor Inc.) and an inverted optical microscope (Ti-E, Nikon Inc.). A linear polarizer (LPNIRE100-B, Thorlabs Inc.) and a quarter-wave

DOI: 10.1021/acsnano.8b02566
ACS Nano 2018, 12, 5030−5041

plate (AQWP10M-980, Thorlabs Inc.) converted an unpolarized light into a circularly polarized light. The handedness of the circularly polarized light was controlled by rotating the fast axis of the quarter-wave plate with respect to the polarization axis of the linear polarizer.

Numerical Simulations. The optical spectra were simulated using a commercially available software package provided by FDTD Solutions, Lumerical Inc. The wavelength-dependent dielectric functions of Au were adapted from Johnson and Christy.[62] The refractive indices of other materials are listed: glass substrate (n = 1.46), as-prepared silk (n = 1.5), silk after swelling (n = 1.4), spin-on glass (n = 1.4), and PMMA (n = 1.485). The total-field scattered-field (TFSF) source generating a plane wave was used to supply incident light. The size of the mesh covering the region of the plasmonic structures was 3 nm. Perfectly matched layers (PMLs) were used as boundaries at all directions. The effective simulation area was set as 5 μm × 5 μm, which covered about 280 nanoholes in each layer of the MCMs. The simulation time and the auto shut-off level were set as 3000 fs and 1×10^{-5} to avoid numerical errors.

ASSOCIATED CONTENT

Supporting Information

The Supporting Information is available free of charge on the ACS Publications website at DOI: 10.1021/acsnano.8b02566.

Additional simulated CD spectra, CPL-dependent near-field coupling, details of analytical fitting, detailed demonstration of fabrication procedures, experimental control of IC1 spacer thickness, CD spectra of silk-MCM in different solvents, switchable color contrast, and ultrasensitive detection of methanol in hexane (PDF)

AUTHOR INFORMATION

Corresponding Author

*E-mail: zheng@austin.utexas.edu.

ORCID

Mingsong Wang: 0000-0001-9071-5517
Jianwen Dong: 0000-0003-2379-554X
Yuebing Zheng: 0000-0002-9168-9477

Notes

The authors declare no competing financial interest.

ACKNOWLEDGMENTS

Z.W., M.W., and Y.Z. acknowledge the financial supports of the Office of Naval Research Young Investigator Program (N00014-17-1-2424) and the Early Career Faculty Award from National Aeronautics and Space Administration (80NSSC17K0520). X.C. and J.D. acknowledge the financial support by Natural Science Foundation of China (11704422). We thank Prof. Tiger Tao and Mike Lee for providing the silk fibroin solutions and the Texas Advanced Computing Center (TACC) at The University of Texas at Austin for providing high-performance computing resources that contributed to the numerical simulations (http://www.tacc.utexas.edu).

REFERENCES

(1) Cui, Y.; Kang, L.; Lan, S.; Rodrigues, S.; Cai, W. Giant Chiral Optical Response from a Twisted-Arc Metamaterial. *Nano Lett.* **2014**, *14*, 1021−1025.

(2) Esposito, M.; Tasco, V.; Todisco, F.; Cuscuna, M.; Benedetti, A.; Sanvitto, D.; Passaseo, A. Triple-Helical Nanowires by Tomographic Rotatory Growth for Chiral Photonics. *Nat. Commun.* **2015**, *6*, 6484.

(3) Gansel, J. K.; Thiel, M.; Rill, M. S.; Decker, M.; Bade, K.; Saile, V.; von Freymann, G.; Linden, S.; Wegener, M. Gold Helix Photonic Metamaterial as Broadband Circular Polarizer. *Science* **2009**, *325*, 1513−1515.

(4) Valev, V. K.; Baumberg, J. J.; Sibilia, C.; Verbiest, T. Chirality and Chiroptical Effects in Plasmonic Nanostructures: Fundamentals, Recent Progress, and Outlook. *Adv. Mater.* **2013**, *25*, 2517−2534.

(5) Verre, R.; Shao, L.; Odebo Lank, N.; Karpinski, P.; Yankovich, A. B.; Antosiewicz, T. J.; Olsson, E.; Kall, M. Metasurfaces and Colloidal Suspensions Composed of 3D Chiral Si Nanoresonators. *Adv. Mater.* **2017**, *29*, 1701352.

(6) Konishi, K.; Bai, B.; Meng, X.; Karvinen, P.; Turunen, J.; Svirko, Y. P.; Kuwata-Gonokami, M. Observation of Extraordinary Optical Activity in Planar Chiral Photonic Crystals. *Opt. Express* **2008**, *16*, 7189−7196.

(7) Vignolini, S.; Yufa, N. A.; Cunha, P. S.; Guldin, S.; Rushkin, I.; Stefik, M.; Hur, K.; Wiesner, U.; Baumberg, J. J.; Steiner, U. A 3D Optical Metamaterial Made by Self-Assembly. *Adv. Mater.* **2012**, *24*, OP23−27.

(8) Khanikaev, A. B.; Arju, N.; Fan, Z.; Purtseladze, D.; Lu, F.; Lee, J.; Sarriugarte, P.; Schnell, M.; Hillenbrand, R.; Belkin, M. A.; et al. Experimental Demonstration of the Microscopic Origin of Circular Dichroism in Two-Dimensional Metamaterials. *Nat. Commun.* **2016**, *7*, 12045.

(9) Cotrufo, M.; Osorio, C. I.; Koenderink, A. F. Spin-Dependent Emission from Arrays of Planar Chiral Nanoantennas Due to Lattice and Localized Plasmon Resonances. *ACS Nano* **2016**, *10*, 3389−3397.

(10) Collins, J. T.; Kuppe, C.; Hooper, D. C.; Sibilia, C.; Centini, M.; Valev, V. K. Chirality and Chiroptical Effects in Metal Nanostructures: Fundamentals and Current Trends. *Adv. Opt. Mater.* **2017**, *5*, 1700182.

(11) Zhao, Y.; Belkin, M. A.; Alu, A. Twisted Optical Metamaterials for Planarized Ultrathin Broadband Circular Polarizers. *Nat. Commun.* **2012**, *3*, 870.

(12) Hendry, E.; Carpy, T.; Johnston, J.; Popland, M.; Mikhaylovskiy, R. V.; Lapthorn, A. J.; Kelly, S. M.; Barron, L. D.; Gadegaard, N.; Kadodwala, M. Ultrasensitive Detection and Characterization of Biomolecules Using Superchiral Fields. *Nat. Nanotechnol.* **2010**, *5*, 783−787.

(13) Ma, W.; Kuang, H.; Xu, L.; Ding, L.; Xu, C.; Wang, L.; Kotov, N. A. Attomolar DNA Detection with Chiral Nanorod Assemblies. *Nat. Commun.* **2013**, *4*, 2689.

(14) Yoo, S.; Park, Q. H. Chiral Light-Matter Interaction in Optical Resonators. *Phys. Rev. Lett.* **2015**, *114*, 203003.

(15) Li, W.; Coppens, Z. J.; Besteiro, L. V.; Wang, W.; Govorov, A. O.; Valentine, J. Circularly Polarized Light Detection with Hot Electrons in Chiral Plasmonic Metamaterials. *Nat. Commun.* **2015**, *6*, 8379.

(16) Kang, L.; Rodrigues, S. P.; Taghinejad, M.; Lan, S.; Lee, K. T.; Liu, Y.; Werner, D. H.; Urbas, A.; Cai, W. Preserving Spin States Upon Reflection: Linear and Nonlinear Responses of a Chiral Meta-Mirror. *Nano Lett.* **2017**, *17*, 7102−7109.

(17) Wang, Z.; Jia, H.; Yao, K.; Cai, W.; Chen, H.; Liu, Y. Circular Dichroism Metamirrors with Near-Perfect Extinction. *ACS Photonics* **2016**, *3*, 2096−2101.

(18) Kim, Y.; Yeom, B.; Arteaga, O.; Jo Yoo, S.; Lee, S. G.; Kim, J. G.; Kotov, N. A. Reconfigurable Chiroptical Nanocomposites with Chirality Transfer from the Macro- to the Nanoscale. *Nat. Mater.* **2016**, *15*, 461−468.

(19) Kim, T.-T.; Oh, S. S.; Kim, H.-D.; Park, H. S.; Hess, O.; Min, B.; Zhang, S. Electrical Access to Critical Coupling of Circularly Polarized Waves in Graphene Chiral Metamaterials. *Sci. Adv.* **2017**, *3*, e1701377.

(20) Kuzyk, A.; Urban, M. J.; Idili, A.; Ricci, F.; Liu, N. Selective Control of Reconfigurable Chiral Plasmonic Metamolecules. *Sci. Adv.* **2017**, *3*, e1602803.

(21) Feringa, B. L.; van Delden, R. A.; Koumura, N.; Geertsema, E. M. Chiroptical Molecular Switches. *Chem. Rev.* **2000**, *100*, 1789−1816.

(22) Fan, R. H.; Zhou, Y.; Ren, X. P.; Peng, R. W.; Jiang, S. C.; Xu, D. H.; Xiong, X.; Huang, X. R.; Wang, M. Freely Tunable Broadband Polarization Rotator for Terahertz Waves. *Adv. Mater.* **2015**, *27*, 1201−1206.

(23) Michel, A.-K. U.; Zalden, P.; Chigrin, D. N.; Wuttig, M.; Lindenberg, A. M.; Taubner, T. Reversible Optical Switching of

DOI: 10.1021/acsnano.8b02566
ACS Nano 2018, 12, 5030−5041

Infrared Antenna Resonances with Ultrathin Phase-Change Layers Using Femtosecond Laser Pulses. *ACS Photonics* **2014**, *1*, 833−839.
(24) Iyer, P. P.; Pendharkar, M.; Palmstrøm, C. J.; Schuller, J. A. Ultrawide Thermal Free-Carrier Tuning of Dielectric Antennas Coupled to Epsilon-Near-Zero Substrates. *Nat. Commun.* **2017**, *8*, 472.
(25) Yin, X.; Schaferling, M.; Michel, A. K.; Tittl, A.; Wuttig, M.; Taubner, T.; Giessen, H. Active Chiral Plasmonics. *Nano Lett.* **2015**, *15*, 4255−4260.
(26) Kuzyk, A.; Schreiber, R.; Zhang, H.; Govorov, A. O.; Liedl, T.; Liu, N. Reconfigurable 3D Plasmonic Metamolecules. *Nat. Mater.* **2014**, *13*, 862−866.
(27) Wang, Z.; Jing, L.; Yao, K.; Yang, Y.; Zheng, B.; Soukoulis, C. M.; Chen, H.; Liu, Y. Origami-Based Reconfigurable Metamaterials for Tunable Chirality. *Adv. Mater.* **2017**, *29*, 1700412.
(28) Wu, Z.; Zheng, Y. Moiré Chiral Metamaterials. *Adv. Opt. Mater.* **2017**, *5*, 1700034.
(29) Johnson, W. C., Jr Secondary Structure of Proteins through Circular Dichroism Spectroscopy. *Annu. Rev. Biophys. Biophys. Chem.* **1988**, *17*, 145−166.
(30) Fan, Z.; Govorov, A. O. Plasmonic Circular Dichroism of Chiral Metal Nanoparticle Assemblies. *Nano Lett.* **2010**, *10*, 2580−2587.
(31) Miyamaru, F.; Hangyo, M. Anomalous Terahertz Transmission through Double-Layer Metal Hole Arrays by Coupling of Surface Plasmon Polaritons. *Phys. Rev. B: Condens. Matter Mater. Phys.* **2005**, *71*, 165408.
(32) Ortuño, R.; García-Meca, C.; Rodríguez-Fortuño, F. J.; Martí, J.; Martínez, A. Role of Surface Plasmon Polaritons on Optical Transmission through Double Layer Metallic Hole Arrays. *Phys. Rev. B: Condens. Matter Mater. Phys.* **2009**, *79*, 075425.
(33) Chang, S.-H.; Gray, S.; Schatz, G. Surface Plasmon Generation and Light Transmission by Isolated Nanoholes and Arrays of Nanoholes in Thin Metal Films. *Opt. Express* **2005**, *13*, 3150−3165.
(34) Kim, C. J.; Sanchez-Castillo, A.; Ziegler, Z.; Ogawa, Y.; Noguez, C.; Park, J. Chiral Atomically Thin Films. *Nat. Nanotechnol.* **2016**, *11*, 520−524.
(35) Christ, A.; Ekinci, Y.; Solak, H. H.; Gippius, N. A.; Tikhodeev, S. G.; Martin, O. J. F. Controlling the Fano Interference in a Plasmonic Lattice. *Phys. Rev. B: Condens. Matter Mater. Phys.* **2007**, *76*, 201405.
(36) Gallinet, B.; Martin, O. J. F. Influence of Electromagnetic Interactions on the Line Shape of Plasmonic Fano Resonances. *ACS Nano* **2011**, *5*, 8999−9008.
(37) Ebbesen, T. W.; Lezec, H. J.; Ghaemi, H. F.; Thio, T.; Wolff, P. A. Extraordinary Optical Transmission through Sub-Wavelength Hole Arrays. *Nature* **1998**, *391*, 667−669.
(38) Martin-Moreno, L.; Garcia-Vidal, F. J.; Lezec, H. J.; Pellerin, K. M.; Thio, T.; Pendry, J. B.; Ebbesen, T. W. Theory of Extraordinary Optical Transmission through Subwavelength Hole Arrays. *Phys. Rev. Lett.* **2001**, *86*, 1114−1117.
(39) Ahmadivand, A.; Gerislioglu, B.; Pala, N. Active Control over the Interplay between the Dark and Hidden Sides of Plasmonics Using Metallodielectric Au−$Ge_2Sb_2Te_5$ Unit Cells. *J. Phys. Chem. C* **2017**, *121*, 19966−19974.
(40) Fan, J. A.; Wu, C.; Bao, K.; Bao, J.; Bardhan, R.; Halas, N. J.; Manoharan, V. N.; Nordlander, P.; Shvets, G.; Capasso, F. Self-Assembled Plasmonic Nanoparticle Clusters. *Science* **2010**, *328*, 1135−1138.
(41) Hao, F.; Sonnefraud, Y.; Dorpe, P. V.; Maier, S. A.; Halas, N. J.; Nordlander, P. Symmetry Breaking in Plasmonic Nanocavities: Subradiant LSPR Sensing and a Tunable Fano Resonance. *Nano Lett.* **2008**, *8*, 3983−3988.
(42) Kelly, C.; Khosravi Khorashad, L.; Gadegaard, N.; Barron, L. D.; Govorov, A. O.; Karimullah, A. S.; Kadodwala, M. Controlling Metamaterial Transparency with Superchiral Fields. *ACS Photonics* **2018**, *5*, 535−543.
(43) Tassin, P.; Zhang, L.; Zhao, R.; Jain, A.; Koschny, T.; Soukoulis, C. M. Electromagnetically Induced Transparency and Absorption in Metamaterials: The Radiating Two-Oscillator Model and Its Experimental Confirmation. *Phys. Rev. Lett.* **2012**, *109*, 187401.
(44) Zhang, S.; Genov, D. A.; Wang, Y.; Liu, M.; Zhang, X. Plasmon-Induced Transparency in Metamaterials. *Phys. Rev. Lett.* **2008**, *101*, 047401.
(45) Limonov, M. F.; Rybin, M. V.; Poddubny, A. N.; Kivshar, Y. S. Fano Resonances in Photonics. *Nat. Photonics* **2017**, *11*, 543−554.
(46) Luk'yanchuk, B.; Zheludev, N. I.; Maier, S. A.; Halas, N. J.; Nordlander, P.; Giessen, H.; Chong, C. T. The Fano Resonance in Plasmonic Nanostructures and Metamaterials. *Nat. Mater.* **2010**, *9*, 707−715.
(47) Verellen, N.; Sonnefraud, Y.; Sobhani, H.; Hao, F.; Moshchalkov, V. V.; Dorpe, P. V.; Nordlander, P.; Maier, S. A. Fano Resonances in Individual Coherent Plasmonic Nanocavities. *Nano Lett.* **2009**, *9*, 1663−1667.
(48) Karimullah, A. S.; Jack, C.; Tullius, R.; Rotello, V. M.; Cooke, G.; Gadegaard, N.; Barron, L. D.; Kadodwala, M. Disposable Plasmonics: Plastic Templated Plasmonic Metamaterials with Tunable Chirality. *Adv. Mater.* **2015**, *27*, 5610−5616.
(49) Garcia-Vidal, F. J.; Martin-Moreno, L.; Ebbesen, T. W.; Kuipers, L. Light Passing through Subwavelength Apertures. *Rev. Mod. Phys.* **2010**, *82*, 729−787.
(50) de León-Pérez, F.; Brucoli, G.; García-Vidal, F. J.; Martín-Moreno, L. Theory on the Scattering of Light and Surface Plasmon Polaritons by Arrays of Holes and Dimples in a Metal Film. *New J. Phys.* **2008**, *10*, 105017.
(51) Li, T.; Liu, H.; Wang, F. M.; Li, J. Q.; Zhu, Y. Y.; Zhu, S. N. Surface-Plasmon-Induced Optical Magnetic Response in Perforated Trilayer Metamaterial. *Phys. Rev. E* **2007**, *76*, 016606.
(52) Zhang, S.; Fan, W.; Panoiu, N. C.; Malloy, K. J.; Osgood, R. M.; Brueck, S. R. J. Experimental Demonstration of Near-Infrared Negative-Index Metamaterials. *Phys. Rev. Lett.* **2005**, *95*, 137404.
(53) Zheng, X.; Zhao, Z.; Peng, W.; Zhang, J.; Zhao, H.; Shi, W. Tuning the Terahertz Trapped Modes of Conductively Coupled Fano-Resonators in Reflectional and Rotational Symmetry. *Opt. Mater. Express* **2018**, *8*, 105−118.
(54) Clerk, A. A.; Waintal, X.; Brouwer, P. W. Fano Resonances as a Probe of Phase Coherence in Quantum Dots. *Phys. Rev. Lett.* **2001**, *86*, 4636−4639.
(55) Klar, T.; Perner, M.; Grosse, S.; von Plessen, G.; Spirkl, W.; Feldmann, J. Surface-Plasmon Resonances in Single Metallic Nanoparticles. *Phys. Rev. Lett.* **1998**, *80*, 4249−4252.
(56) Stietz, F.; Bosbach, J.; Wenzel, T.; Vartanyan, T.; Goldmann, A.; Träger, F. Decay Times of Surface Plasmon Excitation in Metal Nanoparticles by Persistent Spectral Hole Burning. *Phys. Rev. Lett.* **2000**, *84*, 5644−5647.
(57) Lee, M.; Jeon, H.; Kim, S. A Highly Tunable and Fully Biocompatible Silk Nanoplasmonic Optical Sensor. *Nano Lett.* **2015**, *15*, 3358.
(58) Kim, S.; Mitropoulos, A. N.; Spitzberg, J. D.; Tao, H.; Kaplan, D. L.; Omenetto, F. G. Silk Inverse Opals. *Nat. Photonics* **2012**, *6*, 818−823.
(59) Duan, X.; Kamin, S.; Sterl, F.; Giessen, H.; Liu, N. Hydrogen-Regulated Chiral Nanoplasmonics. *Nano Lett.* **2016**, *16*, 1462−1466.
(60) Jeong, H. H.; Mark, A. G.; Alarcon-Correa, M.; Kim, I.; Oswald, P.; Lee, T. C.; Fischer, P. Dispersion and Shape Engineered Plasmonic Nanosensors. *Nat. Commun.* **2016**, *7*, 11331.
(61) Yeatman, E. M. Resolution and Sensitivity in Surface Plasmon Microscopy and Sensing. *Biosens. Bioelectron.* **1996**, *11*, 635−649.
(62) Johnson, P. B.; Christy, R.-W. Optical Constants of the Noble Metals. *Phys. Rev. B* **1972**, *6*, 4370.

DOI: 10.1021/acsnano.8b02566
ACS Nano 2018, 12, 5030−5041